The University of Texas at Austin
Biomedical Engineering
Cockrell School of Engineering

The University of Texas at Austin
Dell Medical School

Systematic Evaluation of a Method Employing Quantitative MRI to Characterize Vascular Morphological and Functional Features *via* a Dynamic Digital Phantom

Chengyue Wu[1], David A. Hormuth[2], Ty Easley[3], Federico Pineda[4], Victor Eijkhout[5], Gregory S. Karczmar[4], Robert D. Moser[2,6], Thomas E. Yankeelov[1,2,7,8]

Departments of [1]Biomedical Engineering, [6]Mechanical Engineering, [7]Diagnostic Medicine, [8]Oncology, [2]Institute for Computational Engineering and Sciences, [5]Texas Advanced Computing Center, The University of Texas at Austin; [3]Departments of Biomedical Engineering, Washington University in St. Louis; [4]Department of Radiology, The University of Chicago

ODEN INSTITUTE FOR COMPUTATIONAL ENGINEERING & SCIENCES

THE CENTER FOR COMPUTATIONAL ONCOLOGY

Introduction

- We have previously developed image processing and computational modeling methods to characterize patient-specific tumor-associated vasculature[1] and hemodynamics[2].
- Quantitative evaluation of the ability of image processing methods to perform as designed is important but challenging.
- Employing virtual MR simulation on a dynamic digital phantom of contrast agent perfusion and extravasation can help systematically evaluate the sensitivity of developed quantitative MRI methods[1-2] to image quality, including spatial resolution, temporal resolution, and SNR.
- **Overall goal:**

Develop a framework based on a dynamic digital phantom and virtual simulation to rigorously determine an acquisition-reconstruction protocol that can be implemented in the routine clinical setting, thereby enabling the developed quantitative MRI analyses to be widely available.

Methods

There are three major steps in the virtual simulation based on dynamic digital phantom.

Step 1: Geometric model of digital phantom

- Geometry of the digital phantom constructed from the ultra-high spatial resolution (31 μm isotropic voxel) MR data of a male Sprague-Dawley aged (52 weeks) rat kidney[3].
- Segment the whole kidney tissue from the T_1-w image[4]
- Construct the vascular skeleton using tracking approach in the T_2*-w image[4] and automatically determine the local radius.

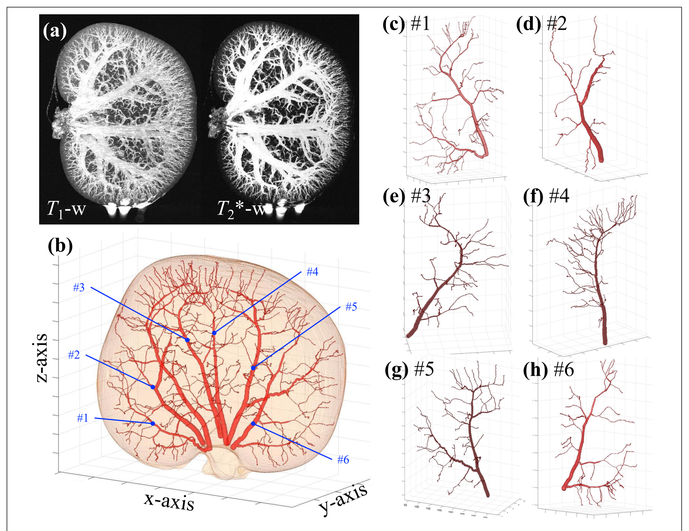

Figure 1. Geometric model of the digital phantom. Panel (a) shows the MIP of ultra-high spatial resolution MRI data. And Panel (b) presents the 3D rendering of the whole vasculature, with the kidney as semi-translucent volume. Panels (g) – (h) shows the individual renal arterial trees, respectively corresponding to the labels (blue) in the panel (a).

Step 2: Dynamic model of digital phantom

- Realistic physiological properties assigned on mesh
- Steady-state flow environment modelled with a 1D-3D coupling CFD system[2]

- Blood flow (Poiseuille's law):

$$Q_v = -\frac{\pi R^4}{8\mu}\cdot\frac{dp_v}{dl}, \quad \boldsymbol{x} \in \Omega_t$$

- Interstitial flow (Darcy's law):

$$\boldsymbol{u}_t = -\kappa \nabla p_t, \quad l \in \Lambda$$

- Fluid exchange (Starling's law):

$$q_e = L_p \cdot \left(p_v - p_{t,ev}\right),$$

$$\boldsymbol{n}_t \cdot \boldsymbol{u}_t = -q_e \qquad l \in \Lambda$$

- CA delivery modelled with an advection-diffusion equation

- Bolus propagation through vasculature:

$$C_p(t, l) = C_{p,0}(t - \tau(l)), \quad l \in \Lambda$$

- delivery through extravascular tissue:

$$\partial C_t/\partial t = -\boldsymbol{u}_t \cdot \nabla C_t + \nabla \cdot (D \nabla C_t) + S, \ \boldsymbol{x} \in \Omega_t$$

with $S = P(C_p - C_t)$, $l \in \Lambda$

Nominations:
Ω_t: tissue domain (3D)
Λ: vascular domain (pseudo-1D)
$\boldsymbol{x}$: 3D coordinate in tissue
l: 1D coordinate along vasculature

R: vascular radius
μ: dynamic viscosity of blood
L_p: vascular hydraulic conductivity
κ: tissue hydraulic conductivity
Q_v: blood flow rate
p_v: blood pressure
q_e: vascular extract flow rate
p_t: interstitial pressure in the tissue
$\boldsymbol{u}_t$: interstitial flow velocity
$p_{t,ev}$: exterior pressure on vessel surface

$C_{p,0}$: initial arterial input function
C_p: local vascular CA concentration
C_t: tissue CA concentration
S: source term defined along vessels
D: tissue diffusivity
P: vascular apparent permeability

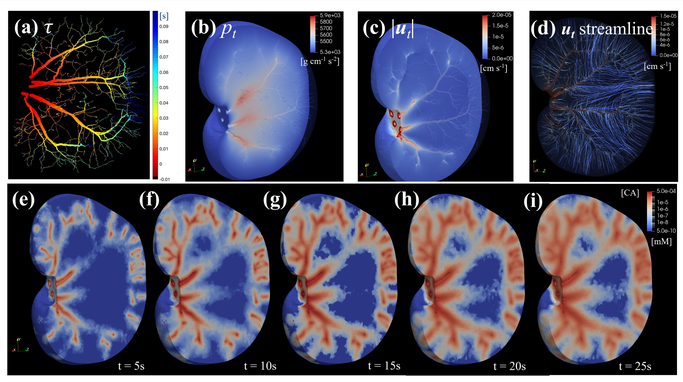

Figure 2. Dynamics of the digital phantom. Panel (a) present MIP of the calculated bolus-arrival time (τ) in the coronal orientation, which indicated the blood flow direction. Panels (b) – (d) present the interstitial pressure, magnitude and streamlines of interstitial flow velocity in the extravascular space of the kidney tissue. Panels (e) – (i) show the spatial distribution of contrast agent concentration at 5 s, 10 s, 15 s, 20 s, and 25 s after the initial delivery of the bolus, respectively.

Step3: Virtual Simulation

- The virtual simulator[5] is illustrated as **Fig 3**

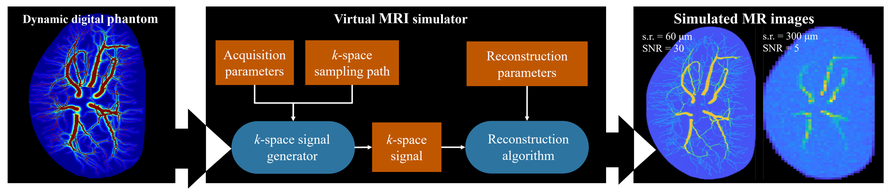

Figure 3. Illustration of virtual MRI simulation. The virtual simulator take the spatiotemporal-resolved digital phantom as input and generate k-space signal with specific acquisition and k-space sampling setting. The generated k-space signal is imported into the optimization-based reconstruction algorithm to produce eventual simulated DCE-MR images with varying spatiotemporal resolutions and SNRs.

- Acquire k-space signal with continuously updated status of digital phantom
- Collect the center of k-space as spatial down-sampling
- Optimization-based image reconstruction allows higher reconstructed temporal resolution than simple IFFT[5]

Let $\boldsymbol{X}$ to be the true images, $\hat{\boldsymbol{X}}$ to be the reconstructed images, $\boldsymbol{Y}$ to be the k-space signal, the measuring domain in k-space of this simulator defined as

$$\boldsymbol{K} = \cup_{t\in\{1,2,\ldots,T\}} (\boldsymbol{K}_t \times \{t\}) \subset \{1, 2, \ldots, n\} \times \{1, 2, \ldots, T\},$$

where $\boldsymbol{K}_t$ is the sampled points in k-space at the time t

$n = n_x \cdot n_y \cdot n_z$ is the total number of points in k-space, determined by matrix size n_x, n_y and n_z

T is the total number of time points in the reconstructed images

Then the reconstruction procedure can be implemented as maximizing smoothness of reconstructed signal over time, i.e.

$$\text{argmin}_{\hat{\boldsymbol{X}}} \{\hat{\boldsymbol{X}}\, \boldsymbol{C}\, \hat{\boldsymbol{X}}' \mid \mathscr{F}(\hat{\boldsymbol{X}})_{\boldsymbol{K}} = \boldsymbol{Y}_{\boldsymbol{K}}\},$$

Where $\mathscr{F}$ represents the Fourier transform

$\boldsymbol{C}$ is the smoothness penalty matrix over time

Eventually solve the optimization problem via preconditioned conjugated gradient descent method.

Results

Simulated images

- Simulate DCE-MR images of 5 pre-contrast frames and 1-min post-contrast scanning with an array of spatial resolutions (s.r. = 30 to 300 μm, isotropic voxel), temporal resolutions (t.r. = 1 to 10 s) and SNRs (= 5 to 75).
- Examples of simulated images and time courses are presented in **Fig 4**.

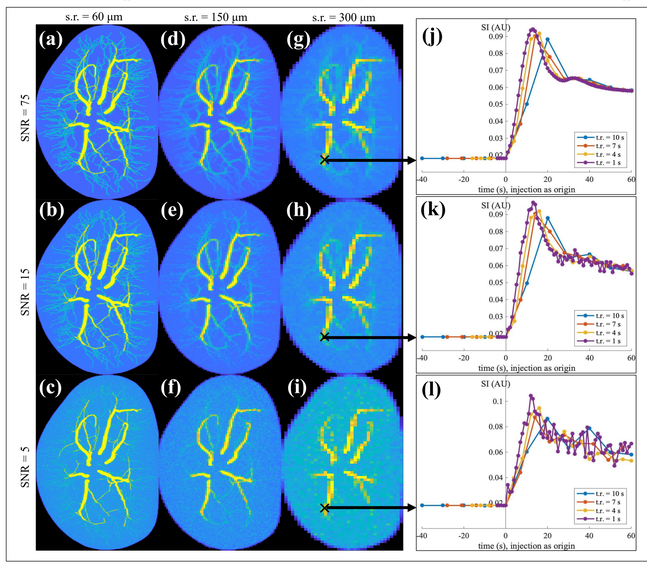

Figure 4. Simulated MR images obtained with various combinations of spatial resolution and signal-to-noise ratio (SNR). Panels (a) – (c) are the maximum intensity projections (MIPs) of the simulated images at 10 s after injection with a spatial resolution of 60 μm and SNRs of 75, 15, and 5, respectively. Similarly, panels (d) – (f) are the MIPs of the simulated images with a spatial resolution of 150 μm and SNRs of 75, 15, and 5, respectively. And panels (g) – (i) are the MIPs of the simulated images with a spatial resolution of 300 μm and SNRs of 75, 15, and 5, respectively. From the datasets with the spatial resolution of 300 μm, one artery voxel is picked to show simulated time courses. Specifically, panels (j) – (l) shows the one-voxel time courses obtained with varying temporal resolutions (t.r. = 1 s, 4 s, 7 s, 10 s) with the SNRs of 75, 15, and 5, respectively.

- Observation of contrast-to-noise ratios (CNR, i.e. the ratio of median value in vessel ROIs to the standard deviation in non-vessel ROIs) indicates that the contrast of micro-vasculature to the background are significantly affected by both the down-sampling and increasing of noise.
  - CNR = 16.99, 10.29, 6.90 for SNR = 30 and s.r. = 60 μm, 150 μm, and 300 μm
  - CNR = 9.47, 7.36, 5.65 for SNR = 5 and s.r. = 60 μm, 150 μm, and 300 μm
- Capture of the peak and width of vascular bolus are significantly affected by the temporal resolution.

Evaluation of morphological analysis

- All the morphological analyses evaluated are much more sensitive to the spatial resolution than to the SNR.
- **Measure #1:** Accuracy of segmented vessel centerlines

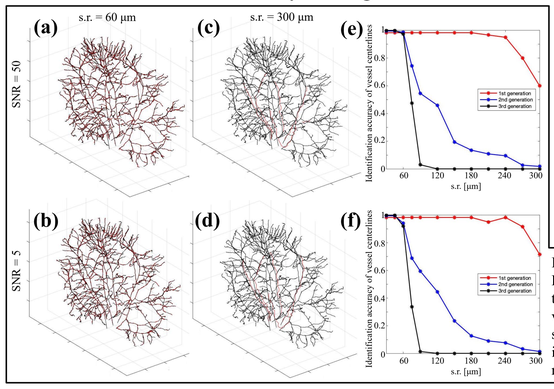

- **IA**: portion of vessels in certain generation that can be accurately segmented comparing to true vasculature.
- Major vessels in the vasculature (i.e. 1st generation) can be preserved with accuracy above 95% for s.r. up to 240 μm.
- Small branches and arterioles (i.e. 2nd and 3rd generations) can only be preserved with 95% accuracy for s.r. up to 60 μm.

Figure 5. Accuracy of identifying vessel centerlines. Panels (a) – (d) compare the example 3D rendering of the true (black) centerlines of vasculature and segmented (red) vasculature from the images with SNRs of 50 and 5, and s.r. of 60 μm and 300 μm. Panels (e) – (f) present the identification accuracy (IA) of segmented vasculature regarding each generation.

- **Measure #2:** Accuracy of vascular connective structure

- **GED**: cost of edits (add or remove vessels) needed to transform the segmented into true vasculature
- In the spatial resolutions where small branches of vasculature can be seen, gap filling algorithm improves the accuracy of the segmented vasculature's connective structure, by approximately 35% for s.r. = 60 μm and 20% for s.r. = 75 μm, respectively.

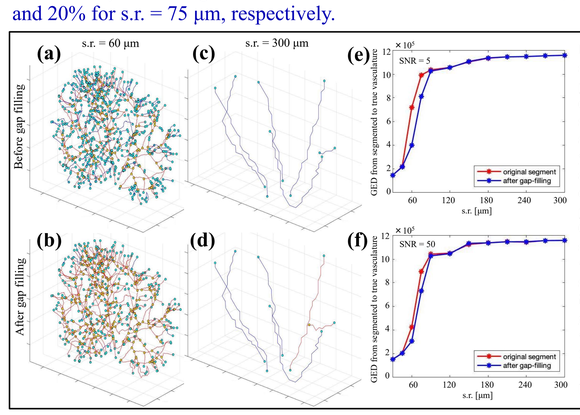

Figure 6. Accuracy of connective structure of the segmented vasculature and the effect of gap filling process. Panels (a) – (b) show the graphs of the connective structure of vasculature originally segmented from data with SNR of 70 and s.r. of 60 μm and the corresponded one after filling gaps. The yellow and cyan circles represent the terminal ends and branching points, respectively. The red and blue curves presents the vessels connected to branching points and with two terminal ends, respectively. Comparing panel (b) to panel (c) indicates the process successfully filled most of breaks in the segmented vasculature and reduce the number of isolated vessel segments. Panel (c) – (d) present a similar comparison in the case of s.r. = 300 μm. Panels (e) – (f) present the graph edit distance (GED) from the segmented vasculature before (red) and after gap-filling (blue) to the true vasculature, with SNRs = 5 and 50, respectively. GED measures the structural dissimilarity between the segmented and true vasculature.

- **Measure #3:** Accuracy of identifying tumor-associated vessels (TAVs)

- Randomly generate 60 spherical lesions and apply the detection of tumor-associated vessel for each
- **SDA**: source detection accuracy, portion of detected TAVs with a source matching with the truth.
- **SDB**: spatial detection bias, spatial distance between the detected TAVs and the true ones.
- On average, SDA > 80% when s.r. ≤ 90 μm; when s.r. climbs to 300 μm, SDA falls to approximately 60%.
- On average, SDB ≤ 0.25 mm when s.r. ≤ 60 μm and maintains to be ≤ 1.25 mm with s.r. up to 300 μm.

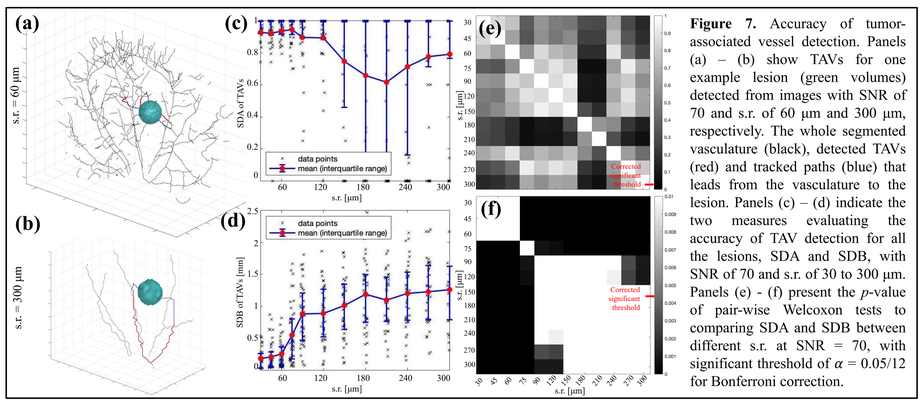

Figure 7. Accuracy of tumor-associated vessel detection. Panels (a) – (b) show TAVs for one example lesion (green volumes) detected from images with SNR of 70 and s.r. of 60 μm and 300 μm, respectively. The whole segmented vasculature (black), detected TAVs (red) and tracked paths (blue) that leads from the vasculature to the lesion. Panels (c) – (d) indicate the two measures evaluating the accuracy of TAV detection for all the lesions, SDA and SDB, with SNR of 70 and s.r. of 30 to 300 μm. Panels (e) - (f) present the p-value of pair-wise Welcoxon tests to comparing SDA and SDB between different s.r. at SNR = 70, with significant threshold of $\alpha = 0.05/12$ for Bonferroni correction.

Discussion & Conclusion

- We developed a digital phantom providing a detailed characterization of vasculature, realistic tissue properties, and physical flow dynamics.
- We established the novel workflow to systematically evaluate quantitative DCE-MRI analysis methods using the digital phantom and virtual simulation of MRI.
- This framework can successfully evaluate the morphological analysis regarding tumor-associated vasculature that developed in our previous work [1].
- **Future directions:**
  - Currently utilizing the framework to evaluate the DCE-MRI-driven pharmacokinetic modeling and hemodynamic analysis.
  - Parallelize the analysis to significantly improve the performance.

References: [1] Wu et al., MRM. 2019;81(3):2147-2160. [2] Wu et al., IEEE-TMI, Feb 2020. [3] Xie et al., Toxicologic pathology. 2012;40(5):764-78. [4] http://www.civm.duhs.duke.edu/lx201107/index.html [5] Easley et al., in Proc. ISMRM 27th Annu. Meeting, Montreal, QC, Canada. May 2019, pp. 1876.

Acknowledgements: NCI U01CA142565, U01CA174706, U24CA226110 and R01 CA218700. CPRIT RR160005. T.E.Y. is a CPRIT Scholar in Cancer Research. MR histology images courtesy of Duke Center for In Vivo Microscopy.

For further information please contact Chengyue Wu (cw35926@utexas.edu) and Thomas Yankeelov (thomas.yankeelov@utexas.edu) **Lab homepage -- http://cco.ices.utexas.edu/**